Check for updates

Pushing the Room Temperature Continuous-Wave Operation Limit of GaSb-Based Interband Cascade Lasers beyond 6 µm

Josephine Nauschütz, Hedwig Knötig, Robert Weih, Julian Scheuermann, Johannes Koeth, Sven Höfling, and Benedikt Schwarz**

GaSb-based interband cascade lasers (ICLs) emitting at a center wavelength of 6.12 µm at 20 °C in continuous-wave operation up to a maximum operating temperature of 40 °C are presented. Pulsed measurements based on broad area devices show improved performance by applying the recently published approach of adjusting the $Ga_{1-x}In_xSb$ layer thickness in the active region to reduce the valence intersubband absorption. The W-quantum well design adjustment and the optimization of the electron injector, to rebalance the electron and hole concentrations in the active quantum wells, improved the device performance, yielding room temperature current densities as low as 0.5 kA cm^{-2} for broad area devices under pulsed operation. As a direct result of this improvement together with optimizations of the waveguide design, the long wavelength limit for GaSb-based ICLs in continuous-wave operation could be extended. For an epi-side down mounted 23 µm wide and 2 mm long device with nine active stages and high-reflectivity back facet, the threshold power is below 1 W and the optical output power is over 25 mW at 20 °C in continuous-wave mode. Such low-threshold and low-power consumption ICLs are especially attractive for mobile and compact sensing systems.

1. Introduction

In 1995 the basic concept of interband cascade lasers (ICLs) was proposed by Rui Q. Yang,[1] with the first experimental demonstration following in 1997.[2] Since then ICLs have emerged as promising light sources for sensor applications in the spectral range between 3–6 µm[3,4] with a performance sweet spot between 3–4 µm. Devices in this range show superior performance, that is, low threshold current densities, high operation temperatures, and comparably high output power. The objective of this paper is to extend the long wavelength limit of GaSb-based ICLs in continuous-wave (cw) operation and improve their performance. An important milestone in ICL performance development was achieved in 2011, addressing the balancing of the internally generated charge carriers via a significant increase of the doping concentration in the electron injector.[5] Recently, a reduction of the valence intersubband absorption has been demonstrated by adjusting the $Ga_{1-x}In_xSb$ hole quantum well (h-QW) thickness, leading to further significant improvement in ICL performance.[6] For GaSb-based ICLs and room temperature (RT) operation, the longest published wavelengths are 6.8 µm for pulsed broad area devices[7] and 5.6 µm for narrow Fabry–Pérot (FP) lasers in cw operation.[8] In the range of 2.8–5.2 µm[9,10] single mode operation was demonstrated at room temperature for devices employing distributed feedback (DFB) gratings. ICLs with wavelengths beyond 6.1 µm have so far been realized by plasmon-enhanced cladding layers on InAs substrates.[11–13] Broad area InAs-based ICLs emit up to 13.2 µm in pulsed operation at 120 K[14] and up to 11 µm at 97 K in cw-operation.[15] The wavelength region around 6 µm is contested by both ICLs and quantum cascade lasers (QCLs), that are also realized in this wavelength window.[16–18] However, QCLs usually show higher threshold current densities and threshold voltages than ICLs. By extending the wavelength range of ICLs beyond 6 µm combined with the low power consumption, we envision that these light sources will successfully compete with QCLs and InAs-based ICLs in low-power applications. The extension of the emission wavelength paves the way towards compact

J. Nauschütz, R. Weih, J. Scheuermann, J. Koeth
nanoplus Nanosystems and Technologies GmbH
Oberer Kirschberg 4, 97218 Gerbrunn, Germany
E-mail: josephine.nauschuetz@nanoplus.com

H. Knötig, B. Schwarz
Institute of Solid State Electronics
TU Wien
Gusshausstrasse 25-25a, 1040 Vienna, Austria
E-mail: benedikt.schwarz@tuwien.ac.at

S. Höfling
Technische Physik
Physikalisches Institut
Universität Würzburg
Am Hubland, 97074 Würzburg, Germany

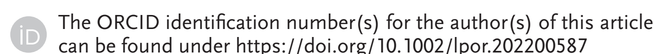

The ORCID identification number(s) for the author(s) of this article can be found under https://doi.org/10.1002/lpor.202200587

© 2023 The Authors. Laser & Photonics Reviews published by Wiley-VCH GmbH. This is an open access article under the terms of the Creative Commons Attribution License, which permits use, distribution and reproduction in any medium, provided the original work is properly cited.

DOI: 10.1002/lpor.202200587

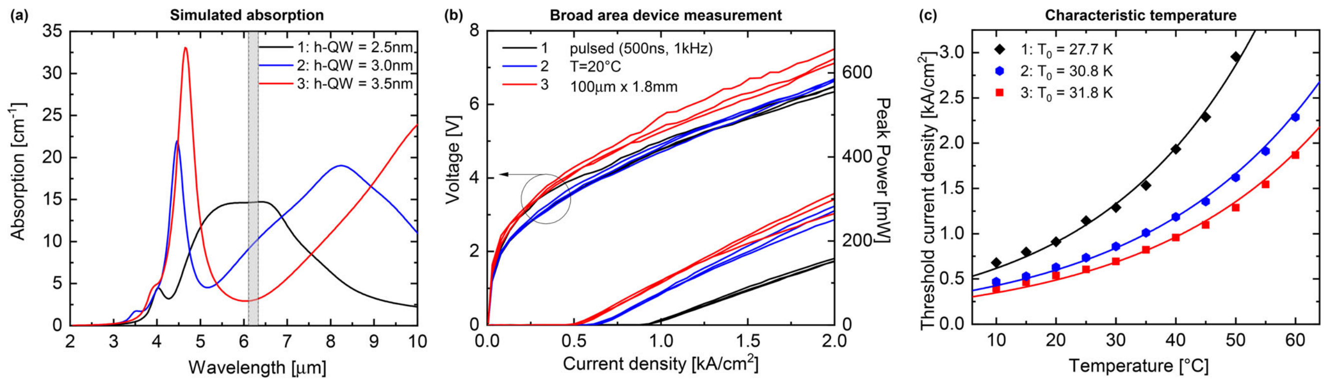

Figure 1. Reduction of intersubband absorption. a) Simulated absorption for sample 1:2.5 nm (black)/sample 2:3.0 nm (blue)/sample 3:3.5 nm (red) $Ga_{0.6}In_{0.4}Sb$ h-QW thicknesses and InAs layers of 2.77/2.31 (1), 2.71/2.26 (2), 2.68/2.24 (3). The examined wavelength range between 6.1 and 6.3 µm is marked. b) Comparison of pulsed *L–I–V* curves for corresponding ICL structures 1–3 with h-QW thicknesses simulated in (a). The data is recorded at low duty cycle (1 kHz, 500 ns) and $T = 20$ °C with broad area devices fully etched through the active region. The devices are not soldered to the heat sink and the facets uncoated. The extracted performance parameters for the best device of each sample can be found in Table 1. The higher threshold current and the low efficiency of sample 1 compared to sample 3 confirm the relationship reflected in the simulation in (a). c) Temperature dependence of the threshold current density for the best broad area device plotted in (b) between 10 and 60 °C with exponential fit to $J_{th}(T)$ and resulting characteristic temperatures T_0.

and mobile analyzers that target further analytes such as NO_2 at 6.25 µm.

2. Results and Discussion

In this work, we describe the three sequential steps we followed to cross the long wavelength limit for GaSb-based ICLs in cw-operation. As a first step and in accordance with the reported causative correlation between valence intersubband absorption and $Ga_{1-x}In_xSb$ h-QW thickness, we investigate the influence of h-QW thickness to reduce the absorption at longer wavelengths. In the second iteration, the electron injector of the active region was optimized by adjusting the doping concentration and shortening it by one InAs/AlSb pair. This stepwise approach is necessary because the valence intersubband absorption is expected to depend on the hole density. Since by varying the doping in the electron injector the hole density is changed in the active W-QW, different optimum values of the doping concentration are expected depending on the strength of the valence intersubband absorption. Therefore, the reduction of absorption needs to be done before the doping concentration can be optimized. In the third part of the optimization process, the waveguide structure was improved by using thicker asymmetric separate confinement layers (SCLs) and thinner cladding layers. Finally, we were able to demonstrate cw operation at RT of an epi-side down mounted Fabry–Pérot laser with a central emission wavelength of 6.12 µm.

2.1. Reduction of Intersubband Absorption

Significant performance improvement at an emission wavelength of 4.35 µm due to the minimization of valence intersubband absorption was demonstrated by Knötig et al.[6] This was achieved by a reduction of the thickness of the $Ga_{1-x}In_xSb$ layer in the active W-QW. Here, we investigate the performance of ICL structures at a wavelength of 6.15 µm. In contrast to the behavior at 4.35 µm, the simulations reveal a reduction of the absorption for wider h-QW thickness. Hence, our study serves two purposes: while tackling the improvement of ICL device performance beyond 6 µm, the relevance of the mitigation of valence intersubband absorption is validated for long wavelength devices. The expected reverse correlation of device performance and h-QW thickness at this wavelength offers the possibility to further explore the effect of valence intersubband absorption experimentally. Following the experimental comparison at an emission wavelength of 4.35 µm, we investigate three h-QW layer thicknesses 2.5 nm (1)/3.0 nm (2)/3.5 nm (3) in the first iteration presented here. The simulated absorption in the W-QW for these three devices targeting an emission wavelength around 6.15 µm is shown in **Figure 1**a. Simulation results are based on the eight-band k·p method using a generalized momentum matrix element model, for more details on the simulation see ref. [6]. Around the emission wavelength (depicted in gray), the widest h-QW (3 - red) should experience the lowest absorption and the narrowest (1 - black) the highest absorption. For a reasonable comparability of the structures, only the thicknesses of the two surrounding InAs layers were adjusted to set the emission wavelength (see Experimental Section). All other parameters in the growth and fabrication of the devices are identical. Figure 1b shows the pulsed light–current–voltage (*L–I–V*) characteristics of the three best broad area devices based on ICL samples 1, 2 and 3 which were etched fully through the active region and were operated at 20 °C and a duty cycle of 0.05%. The simulated correlation between the performance-deteriorating absorption and the h-QW thickness is unequivocally confirmed by the measurements. Significant differences in the measured device performance, like threshold current density J_{th}, output power P_{out}, and efficiency η_{slope}, are observed, with the optimized design 3 showing the best performance. The performance characteristics of the best broad area device of each design are summarized in **Table 1**. The best

© 2023 The Authors. Laser & Photonics Reviews published by Wiley-VCH GmbH
18638899, 2023, 4, Downloaded from https://onlinelibrary.wiley.com/doi/10.1002/lpor.202200587 by Readcube (Labtiva Inc.), Wiley Online Library on [15/01/2024]. See the Terms and Conditions (https://onlinelibrary.wiley.com/terms-and-conditions) on Wiley Online Library for rules of use; OA articles are governed by the applicable Creative Commons License

Table 1. Comparison of laser characteristics of the investigated broad area ICL structures (best device performance): $Ga_{0.6}In_{0.4}Sb$ h-QW thickness, Si-doping concentration in InAs wells of the electron injector, emission wavelength λ, threshold current density J_{th}, threshold voltage V_{th}, optical output power P_{out} at 2 kA cm^{-2} per facet, efficiencies near threshold η_{slope} and characteristic temperature T_0. Performance parameters were measured on 100 µm × 1.8 mm devices, fully etched through the active region, at 20 °C and low duty cycle of 0.05%.

Sample	h-QW [nm]	Doping [cm^{-3}]	λ [µm]	J_{th} [kA cm^{-2}]	V_{th} [V]	P_{out} [mW]	η_{slope} [mW A^{-1}]	T_0 [K]
1	2.5	3E18	6.18	0.92	4.63	159	86	27.7
2	3.0	3E18	6.33	0.63	4.04	284	120	30.8
3	3.5	3E18	6.12	0.53	4.13	314	126	31.8
4	3.0	1E18	6.25	0.50	3.42	319	127	35.9
5	3.5	1E18	6.21	0.52	3.87	390	150	40.2
6	3.5	1E18	6.15	0.50	3.71	382	148	40.2

devices of sample 3 in comparison to sample 1 show a 42% decrease in threshold current density and a doubling of optical output power from 159 to 314 mW at 2 kA cm^{-2}. The difference between performance parameters of samples 2 and 3 is smaller, but also reflects the simulated relationship between h-QW thickness and absorption. It should also be mentioned that the optical output power varies from device to device at high current densities.

In ref. [19] threshold current densities of 0.66–0.80 kA cm^{-2} are reported for broad area lasers at wavelengths around 6.0 µm at 27 °C. With an h-QW width of 3.5 nm and thus reduced W-QW absorption, a comparably low threshold current density of 0.65 kA cm^{-2} (sample 3 - red) was measured at 27 °C. Compared to InAs-based ICLs at 6 µm with 15 active stages,[11] the InAs-based ICLs show lower threshold current density (<0.4 kA cm^{-2}) than the GaSb-based ICL reported here, the threshold voltage of 4.8 V for InAs-ICLs is slightly higher than that for GaSb ICLs with 4.3 V at 27 °C. The InAs-based ICLs do not yet employ adaptions of the h-QW thickness to reduce the intersubband absorption, so adjusting h-QW thickness could lead to performance improvement. The temperature dependence of the threshold current densities for samples 1, 2, and 3 was fitted based on $J_{th}(T) = J_0 \cdot \exp(T/T_0)$ and is plotted in Figure 1c. Measured between 10 and 60 °C, the results demonstrate that sample 3 exhibits the lowest threshold current densities of all three samples 1–3 over the entire temperature range. Moreover, a stronger increase in threshold current density with temperature is observed for sample 1 compared to samples 2 and 3. This behavior fits the simulation result, showing the highest valence intersubband absorption for sample 1. The absorption is expected to depend on the hole density and consequently on the temperature, which is reflected in T_0. Compared to the published T_0 values from ref. [6], the absolute T_0 values here are smaller. It should be noted that the broad area devices in this work are completely etched through the active region to reduce current spreading. Thus, a possible explanation for the difference between T_0 values from deeply-etched and shallowly-etched devices could be a temperature-dependent current spreading.

2.2. Optimization of Electron Injector

The following adjustments of the electron injector aim to more accurately balance the disequilibrium of carrier densities in the W-QW and thereby also reduce loss mechanisms such as Auger recombination.[5] The optimization of the electron injector is implemented after the reduction of the intersubband absorption, due to an expected shift of the optimum value of the doping depending on the presence of this absorption, which depends on the hole density.

Since samples 2 and 3 with h-QW thicknesses of 3.0 and 3.5 nm show lower intersubband absorption than sample 1, the effects of electron injector changes were further examined for these two h-QW thicknesses. For samples 4 and 5 the length of the electron injector was reduced by one InAs/AlSb pair and the layer thicknesses were slightly adjusted. The band structure of the active region for sample 5 is shown in **Figure 2**a. In addition, a main difference between the designs 2/4 and 3/5 is the doping of the electron injector. In samples 4 and 5 the Si-doping concentration in the electron injector was lowered from 3×10^{18} to 1×10^{18} cm^{-3}.

The *L*–*I*–*V* curves of the three best broad area devices of samples 4 and 5 (dashed) are plotted in Figure 2b in comparison to the best devices from samples 2 and 3 (solid). Due to the changes in the electron injector, an improvement in performance can be observed for both h-QW thicknesses. In the case of 3.0 nm with optimized electron injector (sample 4), the performance can be improved to the point where it shows comparable threshold current densities, efficiencies, and output powers as sample 3, which has a 3.5 nm wide h-QW and a longer electron injector with higher doping. For 3.5 nm (sample 5), a threshold current density of 0.6 kA cm^{-2} and a threshold voltage of 4.0 V at 27 °C are obtained, resulting in a threshold power density of 2.4 kW cm^{-2}, which is higher than that of InAs-based ICLs from ref. [11] at similar wavelengths with 1.6–1.9 kW cm^{-2}. In Figure 2b for sample 5, no further reduction of the threshold current density at 20 °C is observed for the adapted electron injector design. However, the design change results in further increased efficiency and optical output power. Indeed, a reduction of the threshold current density for sample 5 is observed at higher temperatures (see Figure 2c). Over a temperature range of 10 to 60 °C the threshold current density was investigated for sample 4 and 5 and is depicted in comparison to sample 2 and 3 in Figure 2c. And throughout the higher temperature range, a decrease in threshold current density due to the changes of the electron injector is observed for both 3.0 nm h-QW thickness, sample 2 (blue) to sample 4 (dashed blue), and 3.5nm h-QW thickness, sample 3 (red) to sample 5 (dashed red). In the low temperature range up to 25 °C, samples 3, 4, and 5 hardly differ. We expected that the change of threshold current density at low temperatures is comparatively small and vanishes within the device-to-device fluctuation. From higher temperatures of approx. 40°C onwards, sample 4 with optimized e-injector displays a slightly lower threshold current density than sample 3 without optimized e-injector. Further systematic investigation with larger numbers of devices is required to understand the effect of the doping on the device performance in detail. In general, sample 5 with optimized h-QW thickness of 3.5 nm and improved e-injector shows the lowest threshold current density

© 2023 The Authors. Laser & Photonics Reviews published by Wiley-VCH GmbH

18638899, 2023, 4, Downloaded from https://onlinelibrary.wiley.com/doi/10.1002/lpor.202200587 by Readcube (Labtiva Inc.), Wiley Online Library on [15/01/2024]. See the Terms and Conditions (https://onlinelibrary.wiley.com/terms-and-conditions) on Wiley Online Library for rules of use; OA articles are governed by the applicable Creative Commons License

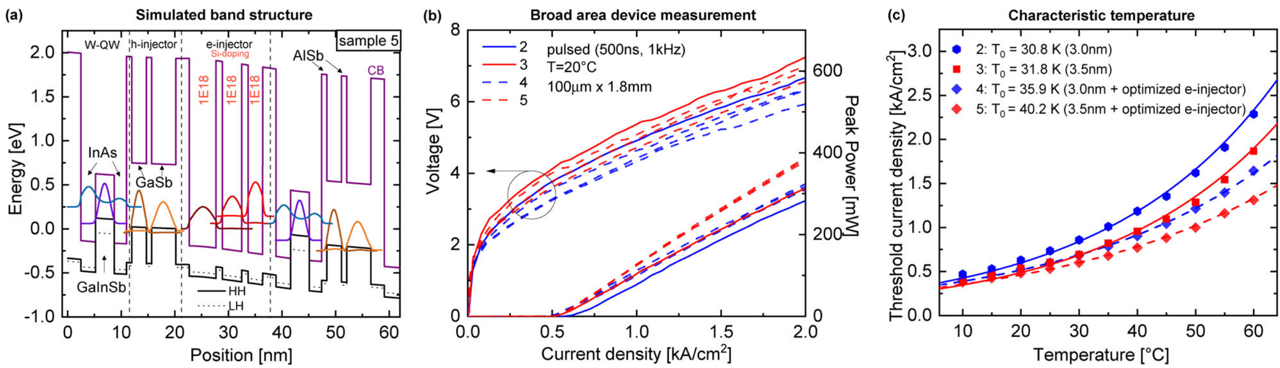

Figure 2. Optimization of electron injector. a) Band structure of sample 5 with probability of presence for electrons and holes (simulated with nextnano[3]) in 1.5 stages of the active region under an applied electric field of 55 kV cm^{-1} for proper alignment of energy levels (conduction band (CB)—purple; valence band (VB)—black (heavy/light hole—solid/dashed). In contrast to samples 1–3, the electron injector is shortened and the doping is reduced to balance the internal carrier densities. b) Comparison of pulsed *L–I–V* curves for corresponding ICL structures 2–5 at low duty cycle and $T = 20$ °C. Samples 2 (blue) and 4 (dashed blue) have an h-QW thickness of 3.0 nm while samples 3 (red) and 5 have a 3.5 nm (dashed red) thick h-QW. The electron injector optimization of samples 4 and 5 improves the performance of the broad area devices attributed to more adequate balancing of charge carrier densities in the W-QW. c) Measured threshold current densities for sample 2–5 at different temperatures (10–60 °C) and corresponding exponential fits to extract the characteristic temperatures T_0 with (dashed) and without (solid) electron injector optimization at two different h-QW thicknesses.

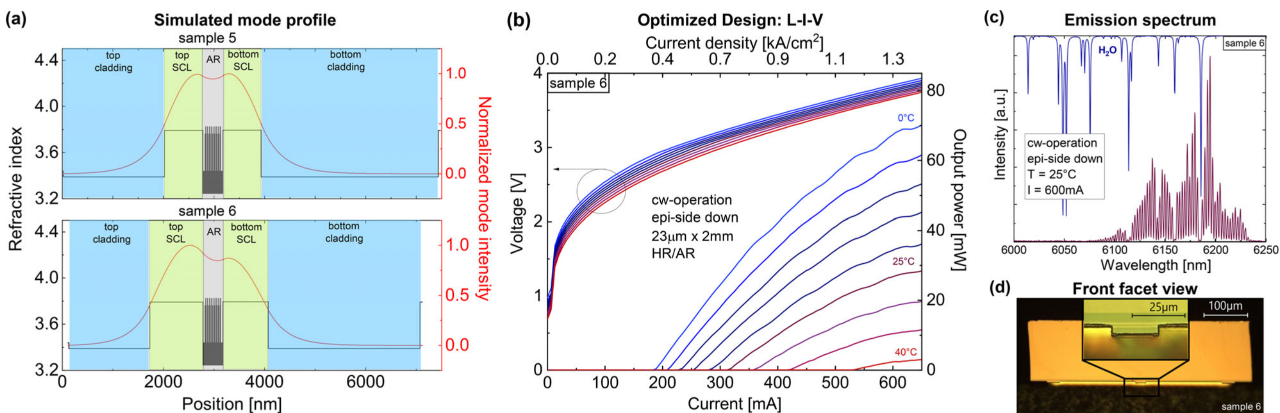

Figure 3. Improved waveguide design. a) Simulation of the vertical field distribution of the optical mode resulting from the refractive index profiles of samples 5 (top) and 6 (bottom). The waveguide design was optimized with asymmetrically thicker SCLs (green) and thinner cladding layers (blue). The normalized mode intensity (red) and the refractive index profile (black) are shown. b) *L–I–V* curves of an epi-side down mounted FP ICL (23 µm wide and 2 mm long—HR back facet / AR front facet) with epitaxy design 6 in cw-mode in steps of 5 °C from 0 to 40 °C. At 0 °C a threshold current density of 420 A cm^{-2} and optical output power of 70 mW is achieved, which correspond to a wallplug efficiency of 3.2%. The small dips in the power curve originate from absorption of water vapor in ambient air. c) Emission spectrum of the epi-side down ICL with a central emission wavelength of 6.17 µm at 25 °C and 600 mA in cw-operation. The dips in the emission spectrum match the absorption peaks of water (blue) very accurately. d) Microscope image of the front facet of this epi-side down ICL soldered on AlN heatspreader with AuSn. In the close-up of the ridge waveguide, the epitaxial structure of the waveguide (SCLs = light yellow; cladding layers = light blue) is visible.

over the entire temperature range and hence the highest characteristic temperature T_0 of 40.2 K of samples 1–5.

2.3. Improved Waveguide Design

As sample 5 shows the best potential for RT-cw-operation due to the highest characteristic temperature, we regrew the active region of sample 5 with an optimized waveguide design (sample 6), see **Figure 3**a. The widths of the cladding layers were reduced and the thickness of the SCLs was asymmetrically increased with a thicker top SCL. This approach is especially beneficial for thermal management, but also for minimization of internal material specific losses, as the GaSb SCLs show higher thermal conductivity and lower internal losses than the cladding layers.[20] The thinner top cladding layer is particularly advantageous for subsequent epi-down mounting, as it allows superior heat dissipation from the device. Moreover the changes in the waveguide design shift the modal overlap from the cladding layers and active region to the SCLs. Comparing the changed waveguide design of sample 6 to sample 5, the optical overlap increases by 8% in the SCLs, and decreases by 6% in the cladding layers and by 2% in the active region according to waveguide simulations. This adjustment of the layer thicknesses reflects a trade-off between the modal gain and the internal losses of the laser structure.[3] Other limiting factors that determine the thickness of the cladding layers are

© 2023 The Authors. Laser & Photonics Reviews published by Wiley-VCH GmbH

18638899, 2023, 4, Downloaded from https://onlinelibrary.wiley.com/doi/10.1002/lpor.202200587 by Readcube (Labtiva Inc.), Wiley Online Library on [15/01/2024]. See the Terms and Conditions (https://onlinelibrary.wiley.com/terms-and-conditions) on Wiley Online Library for rules of use; OA articles are governed by the applicable Creative Commons License

the overlap of the optical mode with the contact metalization and the substrate, which should be small to minimize optical losses. And second, the appearance of leakage modes, which cause periodic losses and can occur if the lower cladding layer is chosen too thin.[21]

In pulsed operation, the deeply etched broad area device shows the same characteristic temperature of 40.2 K as sample 5 (see Figure 2c). This shows a high reproducibility of the growth, since sample 5 and 6 feature the same active region and no further influence on the characteristic temperature due to the changes of the waveguide design were expected at low duty-cycle. Further performance parameters of the broad area device of sample 6 are listed in Table 1.

For performance tests in cw operation, FP lasers (23 μm wide and 2 mm long) with high reflective (HR)/anti-reflective (AR) coating were fabricated from samples 5 and 6 and mounted epi-side down. The comparison of the cw-performance parameters shows an improvement in efficiency by more than 50% from 96 mW A^{-1} (sample 5) to 145 mW A^{-1} (sample 6) at 20 °C due to the changes in the waveguide structure. The maximum operating temperature of sample 5 is 35 °C, which is 5 °C lower than the maximum temperature of sample 6, indicating better heat dissipation in sample 6 with improved waveguide design. In addition, at higher temperatures (25 °C and above), sample 6 shows a lower threshold current than sample 5, demonstrating more efficient operation at higher temperatures. Moreover, sample 5 shows a higher differential resistance of 2.21 Ω, while sample 6 shows only 1.88 Ω (25 °C). The more efficient heat dissipation of sample 6 is also described by the wall-plug efficiency, which is up to 0.8% higher (0 °C) for sample 6 with improved waveguide design. In addition, the thermal resistance of the two samples was estimated from pulsed and cw measurements, resulting in a slightly smaller value of 9.39 K W^{-1} for sample 6 compared to 9.44 K W^{-1} for sample 5 at 30 °C. Although this improvement seems small, the effect is clearly demonstrated by the irrefutably improved cw performance of device 6. The temperature dependent L–I–V characteristics of the device from sample 6 are shown in Figure 3b with a low threshold power of only 0.71 W at 20 °C. Output powers of 70 mW in cw operation at 0 °C were observed, which corresponds to a wallplug efficiency of 3.2%. The cw-emission spectrum at 25 °C with a central emission wavelength of 6.17 μm is plotted in Figure 3c and a close-up of the front facet in Figure 3d.

3. Conclusion

In this paper, the influence of the active $Ga_{1-x}In_xSb$ layer thickness on the device performance for ICLs emitting at 6.1 μm was studied experimentally. Performance improvements by adjusting the h-QW layer thickness reveal the relationship between valence intersubband absorption and $Ga_{1-x}In_xSb$ layer thickness in this wavelength range. This unequivocally proves that the performance improvement when changing the h-QW thickness is indeed due to the avoidance of intersubband resonances in the valence band, as at different wavelengths (4.35 and 6.1 μm) the opposite trend is observed. Hence, the experimental observations nicely match the theoretical results. Moreover, other changes in the band structure, that is, different energy spacing between the hole injector level and the lower lasing level, when varying the h-QW thickness can be excluded as explanations, since these would lead to the same observed behavior for both wavelengths. Broad area devices with reduced absorption show 42% decrease in threshold current density to a record value of 0.5 kA cm^{-2} and a doubling of optical output power in comparison to devices with non adapted h-QW thicknesses. Compared to InAs-based ICLs at the same wavelength from ref. [11] the threshold current density is higher, but the threshold voltage is slightly lower. This results in a smaller threshold power density for InAs-based ICLs from ref. [11] than for the broad area GaSb-based ICLs presented here. It should be noted that the InAs-based ICLs were not optimized by adjusting the h-QW thickness. Therefore, a possible interesting next step would be to investigate how much the InAs-ICLs would benefit from mitigating the valence intersubband absorption. Undoubtedly there is still room for further improvement in device performance for both GaSb- and InAs-based ICLs. Also the design optimization in the electron injector is supported by performance improvements of broad area devices. After reducing the intersubband absorption by adjusting the h-QW thickness, the electron injector was optimized to further balance the carrier densities in the W-QW by using a significantly lower doping concentration and shortening the electron injector. In the last step, the waveguide design was optimized with regard to thermal management and loss minimization. And as a result of this study, laser emission over 6.1 μm with GaSb-based (ICLs) was demonstrated in cw-operation at RT for an epi-side down mounted device with HR back facet. With the presented design strategies, a cw threshold power density of only 1.5 kW cm^{-2} (10 °C) is achieved with a ridge width of 23 μm. In GaSb-based ICLs, the achieved results demonstrate a possible path for the realization of significant performance improvements and are providing a solid basis for future GaSb-based DFB ICLs with excellent device performance at and beyond 6 μm.

4. Experimental Section

All six ICL designs investigated were grown on a Te-doped GaSb substrate by molecular beam epitaxy with nine active stages, see Table 1. In the first three structures 1, 2, and 3, the layer thicknesses of the W-QW were varied as follows: (1) 2.77 nm InAs/2.5 nm $Ga_{0.6}In_{0.4}Sb$/2.31 nm InAs; (2) 2.71 nm InAs/3.0 nm $Ga_{0.6}In_{0.4}Sb$/2.26 nm InAs and (3) 2.68 nm InAs/3.5 nm $Ga_{0.6}In_{0.4}Sb$/2.24 nm InAs. The thicknesses of the InAs layers were adapted with the aim of achieving an emission wavelength of 6.14 μm. The electron injector region was grown with four InAs/AlSb layer pairs, with the three InAs wells closest to the W-QW doped with a Si-concentration of 3×10^{18} cm^{-3}.

The other three structures 4, 5, and 6 were grown with a W-QW thickness of 3.0 nm (4) and 2.68 nm/2.24 nm InAs layers and 3.5 nm (5,6) and 2.72 nm/2.27 nm InAs layers, respectively and also with a $Ga_{1-x}In_xSb$ composition of $x = 0.4$. Moreover, the electron injector consisted of only three InAs/AlSb pairs, where all three InAs wells were doped with a lower Si-concentration of 1×10^{18} cm^{-3}.

All ICL structures except for sample 6 were grown with 760 nm thick SCLs symmetrically arranged around the active stages, while the cladding layers have thicknesses of 2 (top) and 3.5 μm (bottom). Sample 6 has reduced cladding layer thicknesses of 1.6 μm (top)/3.0 μm (bottom) and asymmetrically thicker SCLs with thicknesses of 1050 nm (top)/900 nm (bottom).

For basic characterization of the different ICL structures 1–6, 100 μm wide and 1.8 mm long broad area lasers were fabricated. The ridge

© 2023 The Authors. Laser & Photonics Reviews published by Wiley-VCH GmbH

18638899, 2023, 4, Downloaded from https://onlinelibrary.wiley.com/doi/10.1002/lpor.202200587 by Readcube (Labtiva Inc.), Wiley Online Library on [15/01/2024]. See the Terms and Conditions (https://onlinelibrary.wiley.com/terms-and-conditions) on Wiley Online Library for rules of use; OA articles are governed by the applicable Creative Commons License

Table 2. Refractive indices used to calculate the mode profile in Figure 3a of the individual materials of the ICL structure.

Section	Refractive index
InAs/AlSb-Cladding	3.390
InAs	3.439
AlSb	3.245
GaSb	3.793
$Ga_{0.6}In_{0.4}Sb$	3.825

waveguides were defined by optical lithography and wet etched through the active region using a phosphoric etching solution. The etch depths all lie between 3.8 and 4.0 µm, reaching the lower cladding layer. The metallic top contact served as an etch mask and the backside was coated with an AuGe/Ni/Au contact. The broad area devices were characterized in pulsed mode (1 kHz, 500 ns). The devices were not mounted and the facets were left uncoated.

Ridge waveguides (RWGs) were fabricated from samples 5 and 6 using e-beam lithography and reactive ion etching. Si_3N_4 and SiO_2 passivation layers were deposited and for electrical contacting, the passivation on top of the ridges was removed by reactive ion etching. A Ti-Pt-Au contact was deposited and patterned via a lift-off process. In addition, a 6 µm thick Au layer was electroplated on top. The GaSb substrate was then thinned to 150 µm and coated with an AuGe/Ni/Au backside contact. After cleaving, all lasers were coated with an HR metal layer on the backside and Al_2O_3 AR layer on the front side. 23 µm wide and 2.0 mm long FP lasers were mounted epi-side down with AuSn solder on an AlN heatspreader for efficient heat extraction from the device. Subsequently, the heatspreader was soldered onto a copper heat sink with InSn and characterized in cw-mode.

The simulation of the band structure and the probability of presence for electrons and holes in Figure 2a was performed with the software nextnano^3[22] with the single band effective mass approximation and considering the Varshni parameters.

The simulation of the vertical field distribution of the optical mode in Figure 3a was performed with the software lasim, which was developed by Dr. M. Kamp at the Technical Physics of the University of Würzburg and solves the Helmholtz equation by means of the transfer matrix method. The refractive indices of the individual materials used to calculate are listed in **Table 2**.

Acknowledgements

J.N. and H.K. contributed equally to this work. This project has received funding from the European Research Council (ERC) under the European Union's Horizon 2020 research and innovation program (Grant agreement No. 853014).

The authors acknowledge TU Wien Bibliothek for financial support through its Open Access Funding Programme.

Conflict of Interest

The authors declare no conflict of interest.

Data Availability Statement

The data that support the findings of this study are available from the corresponding author upon reasonable request.

Keywords

6 µm, GaSb, interband cascade lasers

Received: August 3, 2022
Revised: November 5, 2022
Published online: January 31, 2023

[1] R. Q. Yang, *Superlattices Microstruct.* **1995**, *17*, 77.
[2] C.-H. Lin, R. Q. Yang, D. Zhang, S. Murry, S. Pei, A. Allerman, S. Kurtz, *Electron. Lett.* **1997**, *33*, 598.
[3] J. R. Meyer, W. W. Bewley, C. L. Canedy, C. S. Kim, M. Kim, C. D. Merritt, I. Vurgaftman, *Photonics* **2020**, *7*, 75.
[4] I. Vurgaftman, R. Weih, M. Kamp, J. R. Meyer, C. L. Canedy, C. S. Kim, M. Kim, W. W. Bewley, C. D. Merritt, J. Abell, S. Höfling, *J. Phys. D: Appl. Phys.* **2015**, *48*, 123001.
[5] I. Vurgaftman, W. Bewley, C. Canedy, C. Kim, M. Kim, C. Merritt, J. Abell, J. Lindle, J. Meyer, *Nat. Commun.* **2011**, *2*, 585.
[6] H. Knötig, J. Nauschütz, N. Opačak, S. Höfling, J. Koeth, R. Weih, B. Schwarz, *Laser Photonics Rev.* **2022**, *16*, 2200156.
[7] A. Bader, L. Steinbrecher, F. Rothmayr, Y. Rawal, F. Hartmann, A. Pfenning, S. Höfling, in (Ed: M. Strojnik), *Infrared Remote Sensing and Instrumentation XXIX*, Vol. *11830*. SPIE, Bellingham, WA **2021**, pp. 113–122.
[8] W. W. Bewley, C. L. Canedy, C. S. Kim, M. Kim, C. D. Merritt, J. Abell, I. Vurgaftman, J. R. Meyer, *Opt. Express* **2012**, *20*, 3235.
[9] J. Scheuermann, R. Weih, S. Becker, M. Fischer, J. Koeth, S. Höfling, *Opt. Eng.* **2017**, *57*, 011008.
[10] M. von Edlinger, J. Scheuermann, R. Weih, C. Zimmermann, L. Nähle, M. Fischer, J. Koeth, S. Höfling, M. Kamp, *IEEE Photonics Technol. Lett.* **2014**, *26*, 480.
[11] R. Q. Yang, L. Li, W. Huang, S. M. S. Rassel, J. A. Gupta, A. Bezinger, X. Wu, S. G. Razavipour, G. C. Aers, *IEEE J. Sel. Top. Quantum Electron.* **2019**, *25*, 1200108.
[12] S. M. S. Rassel, L. Li, Y. Li, R. Q. Yang, J. A. Gupta, X. Wu, G. C. Aers, *Opt. Eng.* **2017**, *57*, 011021.
[13] M. Dallner, S. Höfling, M. Kamp, *Electron. Lett.* **2013**, *49*, 286.
[14] J. A. Massengale, Y. Shen, R. Q. Yang, S. D. Hawkins, J. F. Klem, *Appl. Phys. Lett.* **2022**, *120*, 091105.
[15] L. Li, H. Ye, Y. Jiang, R. Q. Yang, J. C. Keay, T. D. Mishima, M. B. Santos, M. B. Johnson, *J. Cryst. Growth* **2015**, *425*, 369.
[16] F. Cheng, J. Zhang, Y. Sun, N. Zhuo, S. Zhai, J. Liu, L. Wang, S. Liu, F. Liu, *Opt. Express* **2022**, *30*, 5848.
[17] L. J. Mawst, D. Botez, *IEEE Photonics J.* **2022**, *14*, 1508025.
[18] M. Razeghi, S. Slivken, J. Yu, A. Evans, J. David, *Microelectron. J.* **2003**, *34*, 383.
[19] C. L. Canedy, M. V. Warren, C. D. Merritt, W. W. Bewley, C. S. Kim, M. Kim, I. Vurgaftman, J. R. Meyer, in (Ed: M. Razeghi) *Quantum Sensing and Nano Electronics and Photonics XIV*, Vol. *10111*. SPIE, Bellingham, WA **2017**, pp. 80–86.
[20] I. Vurgaftman, W. W. Bewley, C. L. Canedy, C. S. Kim, M. Kim, J. R. Lindle, C. D. Merritt, J. Abell, J. R. Meyer, *IEEE J. Sel. Top. Quantum Electron.* **2011**, *17*, 1435.
[21] W. Bewley, C. Canedy, C. Kim, I. Vurgaftman, M. Kim, J. Meyer, *Phys. E* **2004**, *20*, 466.
[22] S. Birner, T. Zibold, T. Andlauer, T. Kubis, M. Sabathil, A. Trellakis, P. Vogl, *IEEE Trans. Electron Devices* **2007**, *54*, 2137.

© 2023 The Authors. Laser & Photonics Reviews published by Wiley-VCH GmbH

18638899, 2023, 4, Downloaded from https://onlinelibrary.wiley.com/doi/10.1002/lpor.202200587 by Readcube (Labtiva Inc.), Wiley Online Library on [15/01/2024]. See the Terms and Conditions (https://onlinelibrary.wiley.com/terms-and-conditions) on Wiley Online Library for rules of use; OA articles are governed by the applicable Creative Commons License